A Photoacoustic Imaging Device Using Piezoelectric Micromachined Ultrasound Transducers (PMUTs)

Ajay Dangi, *Member, IEEE*, Christopher Y. Cheng, *Member, IEEE*, Sumit Agrawal, Sudhanshu Tiwari, Gaurav Ramesh Datta, Robert R. Benoit, *Member, IEEE*, Rudra Pratap, *Senior Member, IEEE*, Susan Trolier-McKinstry, *Fellow, IEEE*, and Sri-Rajasekhar Kothapalli

***Abstract*— A linear piezoelectric micromachined ultrasound transducer (PMUT) array was fabricated and integrated into a device for photoacoustic imaging (PAI) of tissue phantoms. The PMUT contained 65 array elements, with each element having 60 diaphragms of 60 μm diameter and 75 μm pitch. A lead zirconate titanate (PZT) thin film was used as the piezoelectric layer. The in-air vibration response of the PMUT array elements showed a first mode resonance between 6 and 8 MHz. Hydrophone measurements showed 16.2 kPa average peak ultrasound pressure output at 7.5 mm from one element excited with 5 V_{pp} input. A receive sensitivity of ~0.48 mV/kPa was observed for a PMUT array element with 0 dB gain. The PMUT array was bonded to a custom-printed circuit board to enable compact integration with an optical fiber bundle for PAI. A broad photoacoustic bandwidth of ~89% was observed for the photoacoustic response captured from absorbing pencil lead targets. Linear scanning of a single element of a PMUT array was performed on different tissue phantoms embedded with light-absorbing targets to successfully demonstrate B-mode PAI using PMUTs.**

Manuscript received October 21, 2019; revised November 20, 2019; accepted November 24, 2019. Date of publication November 27, 2019; date of current version March 25, 2020. This work was supported by the National Institute of Biomedical Imaging and Bioengineering (NIBIB), USA, under Grant R00EB017729-04 (SRK). The work of C. Y. Cheng was supported by the Department of Defense (DoD) through the National Defense Science & Engineering Graduate Fellowship (NDSEG) Program. The work of C. Y. Cheng and S. Trolier-McKinstry was supported by the Center for Nanoscale Science, a Materials Research Science and Engineering Center (MRSEC) supported by the National Science Foundation under Grant DMR-1420620. *(Ajay Dangi and Christopher Cheng are co-first authors.) (Corresponding author: Sri-Rajasekhar Kothapalli.)*

A. Dangi and S. Agrawal are with the Department of Biomedical Engineering, Pennsylvania State University, University Park, PA 16802 USA.

C. Y. Cheng and S. Trolier-McKinstry are with the Department of Materials Science and Engineering and Materials Research Institute, Pennsylvania State University, University Park, PA 16802 USA.

S. Tiwari and R. Pratap are with the Centre for Nano Science and Engineering, Indian Institute of Science, Bengaluru 560012, India.

G. R. Datta is with the Department of Electrical Engineering, Pennsylvania State University, University Park, PA 16802 USA.

R. R. Benoit is with the Sensors and Electron Devices Directorate, U.S. Army Research Laboratory, Adelphi, MD 20783 USA.

S.-R. Kothapalli is with the Department of Biomedical Engineering, Pennsylvania State University, University Park, PA 16802 USA, and also with the Penn State Cancer Institute, Pennsylvania State University, Hershey, PA 17033 USA (e-mail: srkothapalli@psu.edu).

Digital Object Identifier 10.1109/TUFFC.2019.2956463

***Index Terms*— Microelectromechanical systems, piezoelectric micromachined ultrasound transducers (PMUTs), photoacoustic imaging (PAI), ultrasound imaging.**

I. Introduction

OVER the last decade, photoacoustic imaging (PAI) has matured into one of the most promising biomedical imaging modalities. This is due to the continued improvements in the instrumentation and image reconstruction, as well as successful validation for multiple applications at preclinical and translational levels [1]–[7]. In PAI, a pulsed light source illuminates the tissue, which, when absorbed by the target, produces a pressure pulse due to the transient thermoelastic expansion. These pressure pulses can be detected by an ultrasound transducer placed at the surface of the tissue [8]–[10].

PAI offers several benefits over current noninvasive biomedical imaging modalities. First, PAI uses nonionizing radiation and is a safe and cost-effective alternative to standard whole-body imaging modalities, such as magnetic resonance imaging (MRI), positron emission tomography (PET), and computed tomography (CT) [11]. Second, the photoacoustic contrast arises from the optical absorption of the tissue rather than the acoustic impedance mismatch in ultrasound imaging. Thus, PAI can supplement medical diagnostics for conditions where definitive medical diagnoses based on mechanical/anatomical differences alone is not possible, such as detection of vascularization or the oxygen saturation level of hemoglobin [12]. Third, since ultrasound and PAI share the same detection platform, conventional ultrasound imaging systems can be adapted to simultaneously display anatomical ultrasound and photoacoustic contrasts in real time. These capabilities have advanced the clinical translation of PAI for many applications, such as imaging of breast, prostate, ovaries, thyroid, and monitoring Crohn's disease activity [13]–[19].

Recent advances in semiconductor technologies have transformed the computational and electronics backend of ultrasound imaging systems. While these advances have enabled ultrasound imaging devices in portable form, conventional ultrasound array transducers are not well suited for developing ultraportable and wearable devices due to their

bulky size and high-voltage operation [20]. Micromachined ultrasound transducers (MUTs) fabricated on silicon have emerged as an alternative to conventional ultrasound arrays [21]–[29]. Along with on-chip integration and miniaturization, MUTs offer several advantages such as reduction in size and weight, low-cost production due to batch fabrication in foundries, and multifrequency imaging capabilities using a single array [30]. By using packaging techniques such as flip-chip bonding with application-specific integrated circuits (ASICs) spatially matched to the ultrasound array elements, the number of ultrasound channels can be increased dramatically, thus enhancing the real-time volumetric imaging capabilities [31]. In fact, MUTs have already been demonstrated for smartphone integration for fingerprint sensing and handheld probes for B-mode ultrasound imaging [32]–[38].

MUTs are mainly of two types: capacitive MUTs (CMUTs), and piezoelectric MUTs (PMUTs) [39], [40]. Unlike CMUTs, PMUTs can operate at low voltages (<5 V) and do not require a large bias voltage, making CMOS integration much easier. PMUTs can also be impedance matched with typical data acquisition systems designed for bulk ultrasound transducers for preliminary testing when the ASIC integration is not available [34], [35], [39]. CMUTs have already been widely explored for PAI, for example, via tissue phantom experiments [21], [30]–[32], as well as *in vivo* preclinical and clinical translation application for human prostate imaging [15], [19]. While PMUTs have been utilized for ultrasound imaging applications, their potential for PAI is yet to be experimentally explored, particularly for deep-tissue imaging [34], [42].

Theoretical studies have shown that PMUTs are promising for PAI [43], [44]. A preliminary experimental demonstration by Chen *et al.* [45] using an AlN-PMUT array reported detection of weak photoacoustic signals from a black target placed less than a millimeter away from the PMUT in a clear (i.e., no optical or acoustic scattering) medium in a Petri dish when illuminated with a focused light spot. This study pointed to the possibility of using PMUTs for PAI. In addition, AlN-PMUTs were utilized to detect photoacoustic images of targets up to 2–3 cm away in clear agar-gel phantoms [46]. Due to the advantages offered by the PMUT technology, there is a clear need to further understand and demonstrate its capabilities for B-mode PAI in tissue at clinically relevant depths.

In this work, the design, fabrication, and characterization of a $Pb(Zr_{0.52}Ti_{0.48})O_3$ (PZT)-based PMUT array are reported. The PMUT array was integrated into a PAI device with a custom-designed printed circuit board (PCB) and an optical fiber bundle assembly; the resulting system was used to successfully demonstrate B-mode PAI on tissue phantoms for the first time with PMUTs.

II. Device Fabrication and Characterization

A. PMUT Array Fabrication and Packaging

PMUTs usually contain a membrane consisting of a piezoelectric thin film sandwiched between two metal electrodes on a passive elastic layer. When the voltage is applied between the two electrodes, an in-plane mechanical stress is generated in the piezoelectric layer, leading to a bending moment due to the asymmetry in the generated piezoelectric stress across the thickness of the suspended structure. The bending moment causes an out-of-plane vibration of the PMUT structure for a sinusoidal voltage input, thus generating the ultrasound output. Conversely, when the structure vibrates in response to an impinging ultrasound wave, a voltage signal is generated across the piezoelectric layer. Thus, the PMUT can act as both an ultrasound transmitter and receiver.

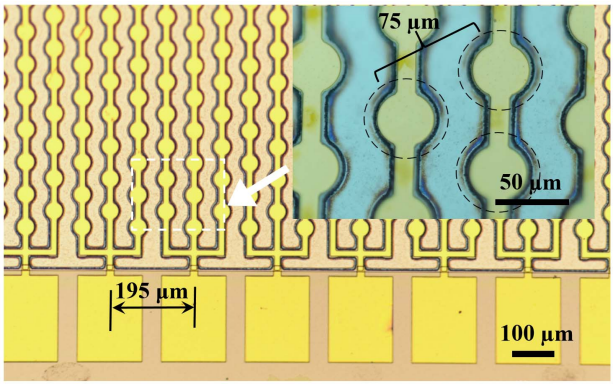

Fig. 1. Optical image of a linear 65-element PMUT array with each element consisting of 60 diaphragms. Inset: center-to-center distance between individual hexagonally packed PMUT diaphragms. Dashed circles: suspended membranes.

Chemical solution-deposited PZT was used as the active piezoelectric material due to its large electromechanical coupling coefficient; the high dielectric permittivity is also helpful in electrical impedance matching with the analog front ends used for conventional ultrasound systems [39]. PMUT diaphragms with 60 μm diameter were selected for this work in order to target an in-air resonance frequency close to 10 MHz. The top electrode was designed to have 65% diameter coverage (diameter of 39 μm) of the diaphragm to improve the performance [20], [21]. The PMUT cells are arranged in a hexagonally packed fashion with a 75 μm center-to-center distance (see Fig. 1). The top electrodes consisted of three columns of 20 PMUT diaphragms, all of which were shorted together to form one PMUT array element, as shown in Fig. 1.

The fabrication process started with a silicon-on-insulator (SOI) wafer with a 2 μm thick Si device layer and 2 μm thick buried thermal oxide layer (Ultrasil Corporation, Hayward, CA, USA). Wet oxidation was used to grow a SiO_2 layer of ~0.16 μm thickness. Then, 30 nm thick Ti was sputtered on the device layer side followed by rapid thermal annealing with 10 sccm of oxygen flow for 15 min at 700 °C and sputtering of 100 nm of Pt at >500 °C, as described elsewhere [48]. In order to achieve highly {001} oriented PZT films, first, a seed layer was deposited by spinning a solution of $Pb(Zr_{0.52}Ti_{0.48})O_3$ doped with 2% Nb with 20 mole percent excess lead (Mitsubishi Materials Corporation, Hyogo, Japan) at 6000 RPM for 30 s. The seed layer was then pyrolyzed at 200 °C for 150 s before crystallization via rapid thermal annealing in a lead-rich environment at 700 °C for 1 min. The film was then spun using 14 mole percent lead excess solution to achieve a $Pb(Zr_{0.52}Ti_{0.48})O_3$ film doped with 2% Nb (Mitsubishi Materials Corporation, Hyogo, Japan)

at 2750 RPM for 45 s. The film was then pyrolyzed at 100 °C for 1 min and 300 °C for 4 min, followed by crystallization in a lead-rich rapid thermal annealer for 1 min at 700 °C. This process was repeated 20 times until a total thickness of 1.9 μm was achieved. A thin layer of 0.08 M PbO solution was spun at 6000 RPM for 45 s with the same pyrolysis and crystallization steps as the aforementioned 20 PZT layers to avoid any pyrochlore phase formation at the top surface of the PZT layer [11]; 2 nm of Ti was then sputtered as an adhesion layer followed by 50 nm of Pt without breaking vacuum for the top electrode. The electrodes were patterned via liftoff and then annealed at 600 °C in air for 1 min to improve the electrode/dielectric interface. Then, 500 nm of Au was deposited using another set of sputtering and liftoff steps on the top electrode to reduce its resistance. Areas not covered by the top electrode were ion milled to gain access to the bottom electrode. Afterward, a 0.9 μm thick bis [benzocyclobutene (BCB)] layer was spun and cured as an insulation layer to reduce parasitic capacitance associated with the fan-out and bonding pads. The bond pad metallization was ~30 nm Ti and 500 nm Au, sputtered without breaking vacuum, and patterned by liftoff. The diaphragms were released via deep reactive-ion etching (DRIE) of the handle of silicon layer from the back of the wafer. The wafer consisting of fabricated PMUT arrays was diced into individual PMUT arrays using a dicing saw. The diced PMUT arrays were characterized and used in the development of the PAI device.

B. PAI Device Design and Integration

As shown in Fig. 2, a PAI device was developed by tightly integrating a custom-made fused silica–silica fiber bundle of 2 m length (Fiberoptics Systems, Simi Valley, CA, USA) and a custom-designed PCB bonded to a linear PMUT array. To start with, an individual PMUT array die was mounted on the PCB with silver paint. The PMUT array was then wire bonded to the PCB and conformally coated with ~4 μm of parylene for waterproofing. The PCB-PMUT assembly was then fixed to the flat surface of the distal (light output) end of the fiber bundle that emits light into the targeted imaging region from two rectangular optical windows of 1.5 mm wide and 30 mm long dimensions, with a ~10 mm gap in between the windows to provide dark-field illumination. The distal end of the fiber bundle, consisting of PCB-PMUT assembly at the center of the two optical windows, is further housed inside a semicylindrical acrylic housing to facilitate transrectal photoacoustic human prostate imaging applications in future. The proximal (input) end of the fiber bundle assembly is connected directly to a wavelength-tunable OPO laser (Phocus Mobile, Opotek Inc., Carlsbad, CA, USA) for PAI experiments.

C. Material Characterization

X-ray diffraction (XRD) and field-emission electron microscopy (FESEM) were used to evaluate the structural quality of the PZT film, while permittivity and hysteresis loops were taken to evaluate the low- and high-field dielectric properties. The results are shown in Fig. 3. It can be seen that highly {100} oriented, phase-pure perovskite PZT was

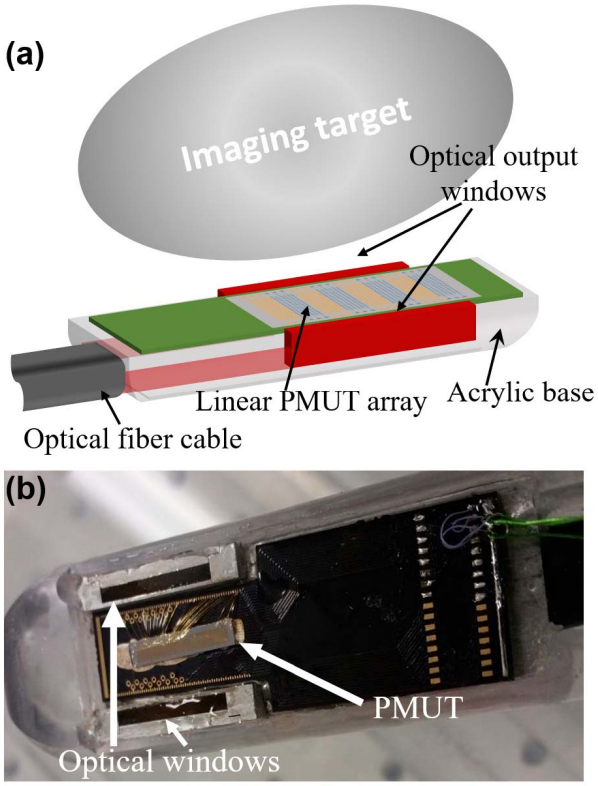

Fig. 2. (a) Schematic of the PMUT-based photoacoustic imaging probe showing the integration of the linear PMUT array with the optical fiber bundles fused to produce two rectangular windows illuminating the imaging target. (b) Schematic of the PMUT array wire-bonded to a PCB and integrated into the light guide apparatus.

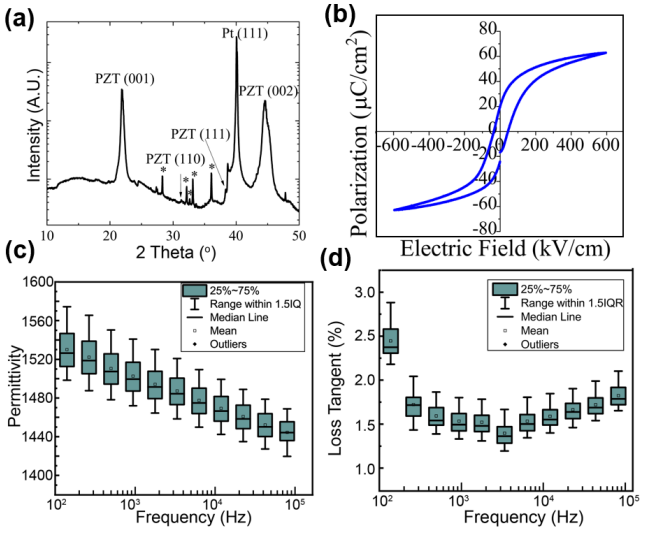

Fig. 3. Evaluation of the PZT via (a) XRD (* indicates substrate peaks) and (b) hysteresis loops. Measurements of (c) permittivity and (d) loss tangent of the thin-film PZT for multiple elements on the PMUT device. Both permittivity and loss tangent showed less than 10% variation for 20 different elements on the same die.

achieved. An average permittivity of 1490 and a mean loss tangent of 1.3% were observed at 1 kHz, with element-to-element standard deviations of 18 and 0.1%, respectively. Hysteresis loops indicate a remnant polarization of ~21 μm/cm^2 and a coercive field of ~50 kV/cm.

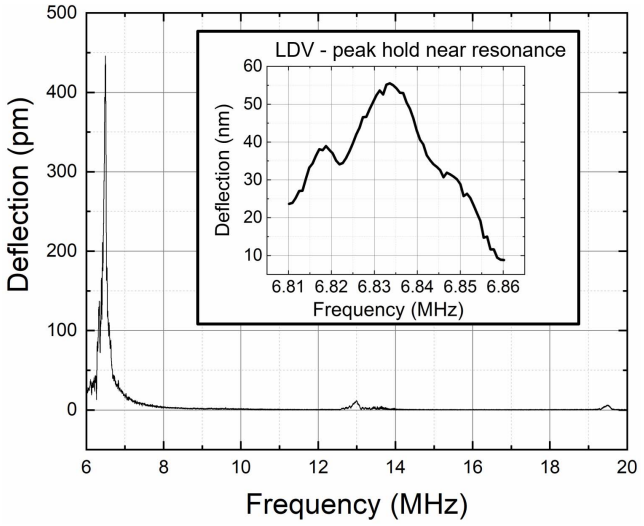

Fig. 4. In-air chirp excitation measurements using laser Doppler vibrometry from a PMUT array element show a first resonant peak between 6.0 and 8.0 MHz. Higher modes can also be seen at ∼13.0 and ∼19.5 MHz. Inset: peak-hold measurements around the first peak, giving ∼55 nm/V deflection sensitivity for the PMUT at resonance.

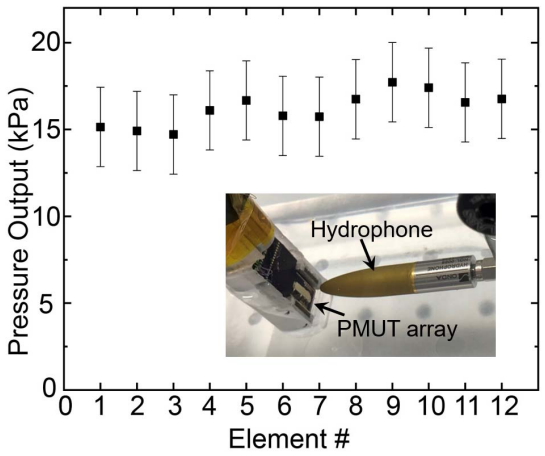

Fig. 5. Pressure output for 12 different PMUT elements in the array at 7.5 mm from the PMUT surface, with each element containing 60 diaphragms excited using a 5 V_{pp} unipolar input. Inset: experimental setup, with the hydrophone ∼7.5 mm distance away from the PMUT.

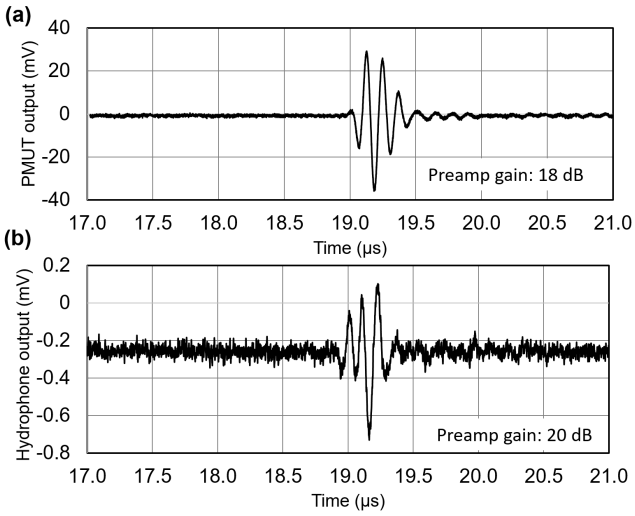

Fig. 6. Receive sensitivity measurements. (a) Voltage output of a PMUT element when excited by a bulk ultrasound transmitter placed 26 mm away and actuated by a single sinusoidal pulse input. (b) Voltage output of a calibrated hydrophone captured at the same location as that of the PMUT measurement.

D. PMUT Vibration and Acoustic Characterization

The PMUT cells were characterized for in-air resonance using a Laser Doppler Vibrometer (LDV) (MSA-500, Polytec GmbH, Waldbronn, Germany). When actuated in air, the first mode resonance was found to lie between 6.0 and 8.0 MHz for PMUTs taken across the wafer. These variations in the first mode resonant frequencies were attributed to variations in the diaphragm size caused by footing from the DRIE process. The frequency range within a die was narrow. A frequency sweep near the resonance for in-air vibrations gives a deflection sensitivity of ∼55 nm/V at the center of a PMUT diaphragm. Higher harmonics were seen near 13.0 and 19.5 MHz, as shown in Fig. 4.

For acoustic characterization, pressure outputs were obtained from 12 different elements of a linear array, with each element having 60 diaphragms. The pressure output for each element was measured by placing the PMUT in an acrylic water tank and operating the PMUT in the transmit mode, while a wideband hydrophone (HGL-0085, Onda Corp., Sunnyvale, CA, USA) acted as a receiver at 7.5 mm distance from the surface of the transducer. The elements were poled at 15 V for 15 min at room temperature prior to the experiments. One element was excited with a unipolar 5 V_{pp} signal at resonance in a five-cycle sinusoidal burst mode. The results are shown in Fig. 5. The output pressure recorded from 12 different elements shows on an average 16.2 kPa output with 0.96 kPa standard deviation.

E. Receive Sensitivity Measurements

Another critical figure-of-merit of ultrasound transducers for PAI applications is the receive sensitivity. To characterize the receive sensitivity of the PMUT, a 0.5 in-diameter single-element bulk ultrasound transducer with 8 MHz center frequency was used as the acoustic source (transmitter). The bulk ultrasound transducer was excited using one cycle of 5 V_{pp} sinusoidal pulse of 8 MHz frequency, generated by an arbitrary waveform generator (SDG6022X, Siglent Technologies, Solon, OH, USA). The ultrasound pressure at 26 mm distance from the transmitter is detected first by different elements of the PMUT array and then using the calibrated hydrophone. Both the PMUT array and the hydrophone were aligned along the longitudinal axis of the transmitter for these measurements. The output of the PMUT was amplified with 18 dB gain using a preamplifier (5073PR, Olympus NDT Inc., Waltham, MA, USA), and the resulting voltage signal was captured using an oscilloscope (MDO3024, Tektronix, Beaverton, OR, USA). Fig. 6(a) shows the voltage output of the PMUT averaged over eight acquisitions giving ∼65 mV peak-to-peak voltage output. Fig. 6(b) shows the voltage output recorded by the hydrophone, which corresponds to ∼17 kPa

peak-to-peak pressure output. The receive sensitivity of the PMUT, estimated by dividing the peak-to-peak voltage output of the PMUT element by the peak-to-peak pressure measured by the hydrophone, was found to be ∼0.48 mV/kPa with 0 dB gain.

III. Photoacoustic Imaging

A. Experimental Setup for PAI

A 32 cm × 18 cm × 12 cm, plastic tank, filled with deionized water was used for the PAI experiments. Phantoms to be imaged were placed at the bottom of the tank; the entire PAI device was submerged with the PMUT array and light output facing the phantom. The distal end of the PAI device was fixed to a motorized three-axis linear stage (NRT100, Thorlabs, Newton, NJ, USA) for alignment. The light pulses (from the laser) propagate through the imaging phantom and are absorbed by chromophores in the phantom, subsequently generating broadband photoacoustic pressure waves due to the transient thermoelastic expansion. The generated photoacoustic pressure is sensed by the PMUT array. In the current experiments, the laser provides a maximum fluence of ∼10 mJ/ cm^2 at 800 nm at the output end of the fiber bundle, which is well within the ANSI safety limits [49]. The voltage output from a single PMUT array element was connected to a commercial preamplifier (5073PR, Olympus NDT Inc., Waltham, MA, USA) providing 39 dB gain. The preamplified output was digitized using a 16-bit data acquisition card (Gage RazorMax16, Dynamic Signals LLC, Lockport, IL, USA) at 1 GSPS in synchronization with each laser pulse.

B-mode PAI requires the ultrasound signals generated by the phantom to be captured by a linear array of ultrasonic receivers with typically 128 or 256 evenly spaced elements. The data acquisition system used for current experiments was limited to four channels. Thus, a linear array acquisition was emulated by linearly scanning the PAI device to 300–500 positions, depending on the size of the phantom, along the length of the device with a 100 μm step size, while the phantom was kept undisturbed. The raw photoacoustic A-line data captured at these positions mimic imaging with a linear array with 100-μm element pitch. The position control of the device was achieved using the linear stage, while MATLAB-based (Mathworks Inc., Natick, MA, USA) control software was used to control the data acquisition and the motion of the linear stage; 20 A-line signals were averaged at each spot in order to reduce the noise floor.

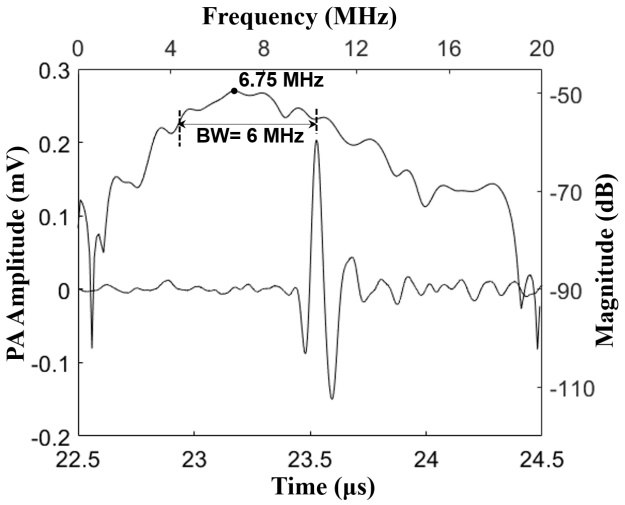

Fig. 7. Photoacoustic signal captured from a pencil lead target shows ∼320 mV peak-to-peak amplitude, after 39 dB gain at the preamplifier stage. The frequency response of the photoacoustic pulse shows a ∼6.75 MHz center frequency with ∼89% bandwidth.

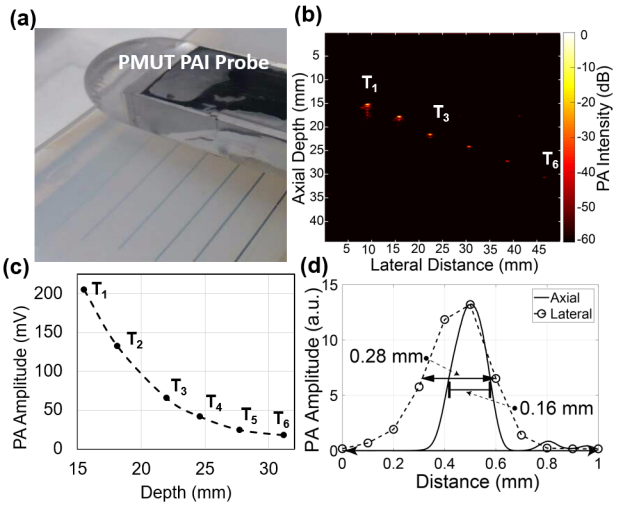

Fig. 8. B-mode photoacoustic imaging of six pencil leads embedded inside agar-gel. (a) Experimental setup showing the agar-gel phantom with six pencil leads at various depths and the PAI device facing the phantom. (b) B-mode photoacoustic image obtained by frequency-domain reconstruction over a 50 mm range with 0.1 mm pitch shows all six pencil leads. (c) Intensity of the photoacoustic signals from the pencil leads reduces as a function of depth inside the phantom. (d) Lateral imaging resolution estimated from the FWHM of the peak intensity at the center of the pencil lead and the axial resolution determined from an envelope function fit over the PA pulse from the pencil lead.

B. Phantom Preparation

The device was tested for PAI capabilities using tissue-mimicking phantoms. First, an agar-gel phantom was prepared by mixing 1.5 g of agarose in 100 mL of deionized water. The solution was heated for 2 min in a standard kitchen microwave. Before solidification, a portion of the solution was poured in a rectangular box, creating a 5 mm thick bed. The base agar-gel pad thus formed was allowed to settle by cooling in a refrigerator for 5 min. One pencil lead with 0.3 mm diameter was placed on the bed and another ∼5 mm thick layer of agar-gel was poured on top. The process was repeated for six layers, resulting in an agar-gel phantom with six pencil leads placed in a diagonal pattern along the depth between 4 and 20 mm [see Fig. 8(a)]. The agar-gel phantom was then placed underwater along with the PMUT. The distance between the PAI device and the top surface of the agar-gel phantom was ∼10 mm.

C. Photoacoustic Characterization and Imaging of Tissue Phantoms

A single A-line signal captured from a pencil lead embedded in agar-gel and aligned for maximum photoacoustic out-

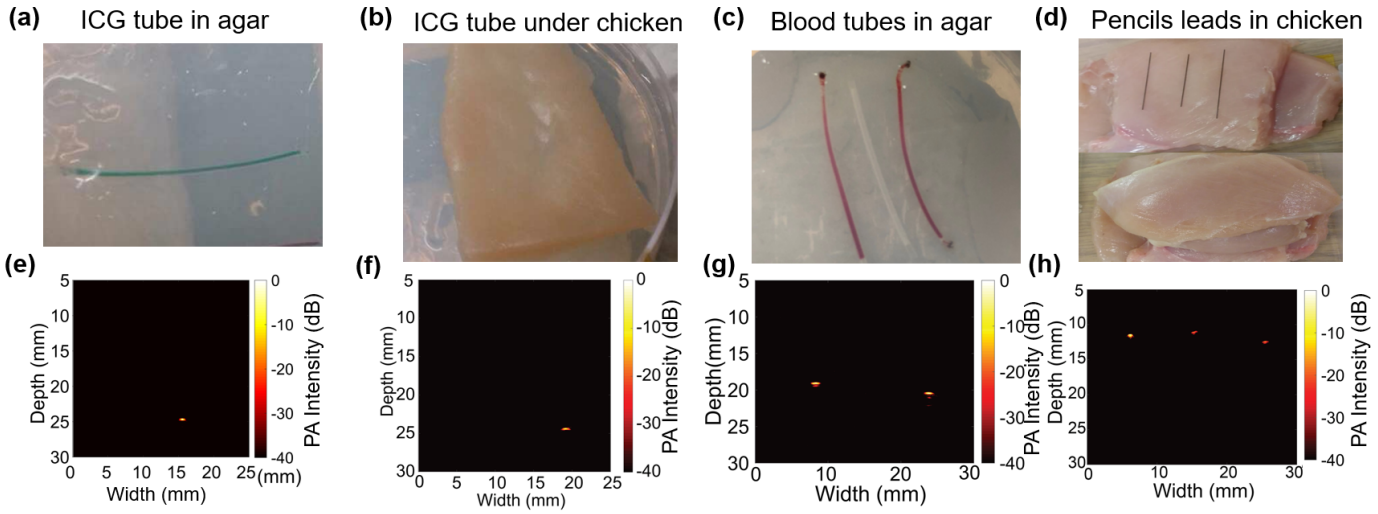

Fig. 9. B-mode photoacoustic imaging (PAI). (a) A clear agar-gel phantom with an ICG-filled tube as target. (b) Phantom shown in (a) is covered with a 2 mm thick chicken tissue layer to introduce scattering of the light. (c) Clear agar-gel phantom with two blood-filled polymer tubes embedded at 5 mm depth with an unfilled tube placed between the two tubes. (d) Pictures showing the preparation of chicken tissue-based phantom. Three 0.3 mm pencil leads were placed on the chicken bed and then an 8 mm thick chicken tissue layer was placed on top of the pencil leads. (e)–(h) are the reconstructed B-mode (photoacoustic images from phantoms shown in (a)–(d), respectively. The color bar for all the reconstructed images represents the photoacoustic intensity, normalized with respect to the maxima within each image, on a log scale with 0 to −40 dB range. All images were acquired using linear scanning of single-element PMUT with 0.1 mm step size.

put is shown in Fig. 7. The photoacoustic pulse received ∼23.5 μs after the laser excitation, matched with the pencil lead at ∼36 mm distance from the PMUT array element, and showed ∼350 mV_{pp} pulse amplitude. Using this single A-line signal, the frequency response of the photoacoustic pulse was found to be ∼6.75 MHz center frequency with ∼89% bandwidth.

Using the PAI device, the agar-gel phantom with six embedded pencil leads was imaged [see Fig. 8(a)]. A Fourier transform-based algorithm was used to reconstruct B-mode images from the raw voltage-time data [11]. Fig. 8(b) shows the reconstructed B-mode photoacoustic image from the 500 signals captured by the PMUT array element while scanning the device over 5 cm with a 0.1 mm pitch. The first four pencil leads, identified as T_1–T_4, were clearly visible. The last two pencil leads T_5 and T_6 were barely visible in the reconstructed PAI image. No time gain compensation was used in the reconstruction algorithm; hence, the reconstructed image is expected to show a depth-dependent decay in the photoacoustic contrast. As expected, a decrease in photoacoustic signal strength as a function of depth of the pencil lead can be seen from the plot in Fig. 8(c). Furthermore, the lateral and axial resolutions were estimated from the full-width at half-maximum (FWHM) of the photoacoustic amplitude of a pencil lead target, T_1, plotted along the horizontal and vertical axes, as shown in Fig. 8(d). The lateral and axial FWHMs for T_1 were found to be ∼0.30 and ∼0.15 mm, respectively. The lateral FWHM was found to increase with depth, reaching up to 0.57 mm for the sixth pencil lead.

Additional PAI experiments were conducted for the four different conditions shown in Fig. 9(a)–(d). First, Fig. 9(a) shows an agar-gel phantom with a polyethylene tube having 1.09 mm outer diameter and 0.38 mm inner diameter filled with a 200 μM indocyanine green (ICG) solution, embedded inside the agar-gel. When the submerged PAI-PMUT probe was aligned directly above the ICG tube phantom, at a ∼20 mm gap, a photoacoustic output of ∼80 mV_{pp} was captured.

Second, the agar-gel phantom with the ICG-filled tube was covered with ∼3 mm of chicken tissue as shown in Fig. 9(b) to induce scattering in the optical illumination. While the photoacoustic signal decreased (the amplitude of the photoacoustic pulse was reduced to ∼30 mV_{pp}), the ICG filled tube was imaged clearly at ∼25 mm distance from the PMUT-PAI device [see Fig. 9(f)].

Third, an imaging phantom consisting of two bovine blood (905-100, Quad Five Inc., Ryegate, MT, USA) filled polyethylene tubes, separated by a clear tube, all of which were embedded in agar-gel, as shown in Fig. 9(c), was investigated as a target. As shown in the reconstructed image in Fig. 9(g), the two blood-filled tubes were detected, while the tube without blood did not generate any above-noise photoacoustic signal due to the lack of absorption.

Finally, the fourth demonstration consisted of imaging pencil lead targets embedded under 8 mm of chicken tissue [see Fig. 9(d) and(h)]. An ∼8 mm thick slice of chicken tissue was used as the bed on which three 0.3 mm pencil leads were placed with ∼15 mm separation, and another ∼8 mm thick chicken slice was placed on the top. Care was taken to minimize any air gap between the layers of chicken tissues and the pencil leads. As shown in the reconstructed photoacoustic image in Fig. 9(h), the three pencil leads could be detected through 8 mm of chicken tissue. For the three pencil leads under chicken, the axial resolutions lie between 0.16 and 0.18 mm and the lateral resolutions lie between 0.30 and 0.50 mm, as estimated using the approach described for Fig. 8(d).

Although the above-mentioned PAI results with the PMUT arrays are encouraging, reducing the noise floor of the PMUTs will improve their photoacoustic sensitivity. Potential sources of noise include cross coupling between neighboring elements, pressure-induced surface, and bulk acoustic waves in the PMUT substrate, the high capacitance of the PMUT element that increases the electrical noise, and the parasitic capacitance introduced by wires connecting the PMUT elements to the imaging system. These noise sources can be reduced by techniques such as the introduction of trenches around the PMUT elements to attenuate substrate vibrations and cross coupling or using lower permittivity materials. Second, it is observed that the receive sensitivity of the PMUT element can vary depending on the poling conditions. The PZT thin film may depole when excited using high-voltage (>5 V) non-unipolar sinusoidal input or when exposed to excessive heat. Hence, it is necessary to ensure uniform poling of the PZT thin film and avoid depoling. Furthermore, delamination was observed between the parylene layer and the top surface of the PMUT diaphragms for a few cases during the poling process or transmit mode operation after repeated use. Such delamination was found to cause sudden degradation in the performance of the PMUT element and needs to be studied further.

IV. Conclusion

Successful fabrication and characterization results of a ~7 MHz linear PMUT array with 89% photoacoustic bandwidth was presented. A compact handheld PAI device was developed by wire-bonding the array to a PCB and further integrating it with a fiber-optic light guide. PAI experiments on different tissue phantoms established the feasibility of imaging photoacoustic contrast from blood, ICG, and pencil leads through scattering tissue using PMUT arrays. These results show, for the first time, the feasibility of a PMUT-based handheld PAI device for imaging targets inside optically and acoustically scattering tissue. Future improvements can be achieved by using ASICs for preamplification and signal conditioning. Also, more complex architectures, such as PMUTs with curved or dome-shaped membranes, can enable higher sensitivities [50], [51]. Low voltage (<10 V) operation, high receive sensitivity, ease of impedance match with conventional ultrasound preamplifiers, and ease of fabrication of miniaturized PMUTs of various shapes and sizes make them attractive for developing multiscale and multimode PAI systems.

References

[1] P. Beard, "Biomedical photoacoustic imaging," *Interface Focus*, vol. 1, pp. 602–631, Aug. 2011.

[2] M. Xu and L. V. Wang, "Photoacoustic imaging in biomedicine," *Rev. Sci. Instrum.*, vol. 77, no. 4, 2006, Art. no. 041101.

[3] L. Xiang, B. Wang, L. Ji, and H. Jiang, "4-D photoacoustic tomography," *Sci. Rep.*, vol. 3, no. 1, p. 1113, Dec. 2013.

[4] K. S. Valluru and J. K. Willmann, "Clinical photoacoustic imaging of cancer," *Ultrasonography*, vol. 35, no. 4, pp. 267–280, 2016.

[5] T. Kitai *et al.*, "Photoacoustic mammography: Initial clinical results," *Breast Cancer*, vol. 21, no. 2, pp. 146–153, Jul. 2012.

[6] B. T. Cox, J. G. Laufer, P. C. Beard, and S. R. Arridge, "Quantitative spectroscopic photoacoustic imaging: A review," *J. Biomed. Opt.*, vol. 17, no. 6, 2012, Art. no. 061202.

[7] L. V. Wang and S. Hu, "Photoacoustic tomography: *In vivo* imaging from organelles to organs," *Science*, vol. 335, no. 6075, pp. 1458–1462, Mar. 2012.

[8] V. Ntziachristos, "Going deeper than microscopy: The optical imaging frontier in biology," *Nature Methods*, vol. 7, pp. 603–614, Jul. 2010.

[9] L. V. Wang, "Multiscale photoacoustic microscopy and computed tomography," *Nature Photon.*, vol. 3, no. 9, pp. 503–509, Sep. 2009.

[10] S. Zackrisson, S. M. W. Y. Van De Ven, and S. S. Gambhir, "Light in and sound out: Emerging translational strategies for photoacoustic imaging," *Cancer Res.*, vol. 74, no. 4, pp. 979–1004, Feb. 2014.

[11] L. M. Denis, G. Esteves, J. Walker, J. L. Jones, and S. Trolier-McKinstry, "Thickness dependent response of domain wall motion in declamped 001 $Pb(Zr_{0.3}Ti_{0.7})O_3$ thin films," *Acta Mater.*, vol. 151, pp. 243–252, Jun. 2018.

[12] I. Stoffels *et al.*, "Metastatic status of sentinel lymph nodes in melanoma determined noninvasively with multispectral optoacoustic imaging.," *Sci. Transl. Med.*, vol. 7, no. 317, Dec. 2015, Art. no. 317ra199.

[13] M. Heijblom, W. Steenbergen, and S. Manohar, "Clinical photoacoustic breast imaging: The twente experience," *IEEE Pulse*, vol. 6, no. 3, pp. 42–46, May/Jun. 2015.

[14] S. R. Kothapalli *et al.*, "Human prostate imaging using a novel integrated transrectal ultrasound and photoacoustic instrument," in *Proc. World Mol. Imaging Congr.*, 2013, vol. 15, no. 1, pp. S1447–S1448.

[15] M. A. Yaseen *et al.*, "Optoacoustic imaging of the prostate: Development toward image-guided biopsy," *Proc. SPIE*, vol. 15, no. 2, 2010, Art. no. 021310.

[16] S. R. Kothapalli, T.-J. Ma, S. Vaithilingam, O. Oralkan, B. T. Khuri-Yakub, and S. S. Gambhir, "Deep tissue photoacoustic imaging using a miniaturized 2-D capacitive micromachined ultrasonic transducer array," *IEEE Trans. Biomed. Eng.*, vol. 59, no. 5, pp. 1199–1204, May 2012.

[17] A. Aguirre, Y. Ardeshirpour, M. M. Sanders, M. Brewer, and Q. Zhu, "Potential role of coregistered photoacoustic and ultrasound imaging in ovarian cancer detection and characterization," *Transl. Oncol.*, vol. 4, no. 1, pp. 29–37, Feb. 2011.

[18] A. Dima and V. Ntziachristos, "*In-vivo* handheld optoacoustic tomography of the human thyroid," *Photoacoustics*, vol. 4, no. 2, pp. 65–69, Jun. 2016.

[19] F. Knieling *et al.*, "Multispectral optoacoustic tomography for assessment of Crohn's disease activity," *New England J. Med.*, vol. 376, no. 13, pp. 1292–1294, Mar. 2017.

[20] J. A. Jensen *et al.*, "SARUS: A synthetic aperture real-time ultrasound system," *IEEE Trans. Ultrason., Ferroelectr., Freq. Control*, vol. 60, no. 9, pp. 1838–1852, Sep. 2013.

[21] Ö. Oralkan *et al.*, "Capacitive micromachined ultrasonic transducers: Next-generation arrays for acoustic imaging," *IEEE Trans. Ultrason., Ferroelectr., Freq. Control*, vol. 49, no. 11, pp. 1596–1610, Nov. 2002.

[22] A. Dangi, A. Hulge, A. Somasundaran, R. S. Valsalam, and R. Pratap, "Complete development of a single cell PMUT transducer: Design, fabrication, characterization, and integration," *J. Inst. Smart Struct. Syst.*, vol. 4, no. 41, pp. 61–69, 2015.

[23] U. Demirci, A. S. Ergun, O. Oralkan, M. Karaman, and B. T. Khuri-Yakub, "Forward-viewing CMUT arrays for medical imaging," *IEEE Trans. Ultrason., Ferroelectr., Freq. Control*, vol. 51, no. 7, pp. 887–895, Jul. 2004.

[24] X. Jiang *et al.*, "Ultrasonic fingerprint sensor with transmit beamforming based on a PMUT array bonded to CMOS circuitry," *IEEE Trans. Ultrason., Ferroelectr., Freq. Control*, vol. 64, no. 9, pp. 1401–1408, Sep. 2017.

[25] Ö. Oralkan *et al.*, "Experimental characterization of collapse-mode CMUT operation," *IEEE Trans. Ultrason., Ferroelectr., Freq. Control*, vol. 53, no. 8, pp. 1513–1523, Aug. 2006.

[26] R. K. W. Chee, A. Sampaleanu, D. Rishi, and R. J. Zemp, "Top orthogonal to bottom electrode (TOBE) 2-D CMUT arrays for 3-D photoacoustic imaging," *IEEE Trans. Ultrason., Ferroelectr., Freq. Control*, vol. 61, no. 8, pp. 1393–1395, Aug. 2014.

[27] B. A. Greenlay and R. J. Zemp, "Fabrication of linear array and top-orthogonal-to-bottom electrode CMUT arrays with a sacrificial release process," *IEEE Trans. Ultrason., Ferroelectr., Freq. Control*, vol. 64, no. 1, pp. 93–107, Jan. 2017.

[28] O. Oralkan *et al.*, "Volumetric ultrasound imaging using 2-D CMUT arrays," *IEEE Trans. Ultrason., Ferroelectr., Freq. Control*, vol. 50, no. 11, pp. 1581–1594, Nov. 2003.

[29] J. Zahorian *et al.*, "Monolithic CMUT-on-CMOS integration for intravascular ultrasound applications," *IEEE Trans. Ultrason., Ferroelectr., Freq. Control*, vol. 58, no. 12, pp. 2659–2667, Dec. 2011.

[30] A. Kshirsagar *et al.*, "Multi-frequency CMUT arrays for imaging-therapy applications," in *Proc. IEEE Int. Ultrason. Symp. (IUS)*, Prague, Czech Republic, Jul. 2013, pp. 1991–1993.
[31] G. Gurun, P. Hasler, and F. L. Degertekin, "Front-end receiver electronics for high-frequency monolithic CMUT-on-CMOS imaging arrays," *IEEE Trans. Ultrason., Ferroelectr., Freq. Control*, vol. 58, no. 8, pp. 1658–1668, Aug. 2011.
[32] X. Jiang *et al.*, "Monolithic ultrasound fingerprint sensor," *Microsyst. Nanoeng.*, vol. 3, p. 17059, Nov. 2017.
[33] H.-Y. Tang *et al.*, "3-D ultrasonic fingerprint sensor-on-a-chip," *IEEE J. Solid-State Circuits*, vol. 51, no. 11, pp. 2522–2533, Nov. 2016.
[34] D. E. Dausch, K. H. Gilchrist, J. B. Carlson, S. D. Hall, J. B. Castellucci, and O. T. V. Ramm, "*In vivo* real-time 3-D intracardiac echo using PMUT arrays," *IEEE Trans. Ultrason., Ferroelectr., Freq. Control*, vol. 61, no. 10, pp. 1754–1764, Oct. 2014.
[35] D. E. Dausch, J. B. Castellucci, D. R. Chou, and O. T. Von Ramm, "Piezoelectric micromachined ultrasound transducer (pMUT) arrays for 3D imaging probes," in *Proc. IEEE Ultrason. Symp.*, vol. 1, Oct. 2006, pp. 930–933.
[36] M. C. Chen *et al.*, "A pixel pitch-matched ultrasound receiver for 3-D photoacoustic imaging with integrated delta-sigma beamformer in 28-nm UTBB FD-SOI," *IEEE J. Solid-State Circuits*, vol. 52, no. 11, pp. 2843–2856, Nov. 2017.
[37] I. O. Wygant *et al.*, "An integrated circuit with transmit beamforming flip-chip bonded to a 2-D CMUT array for 3-D ultrasound imaging.," *IEEE Trans. Ultrason., Ferroelectr., Freq. Control*, vol. 56, no. 10, pp. 2145–2156, Oct. 2009.
[38] D. T. Yeh, O. Oralkan, I. O. Wygant, M. O'Donnell, and B. T. Khuri-Yakub, "3-D Ultrasound imaging using a forward-looking CMUT ring array for intravascular/intracardiac applications," *IEEE Trans. Ultrason., Ferroelectr., Freq. Control*, vol. 53, no. 6, pp. 1202–1211, Jun. 2006.
[39] Y. Qiu *et al.*, "Piezoelectric micromachined ultrasound transducer (PMUT) arrays for integrated sensing, actuation and imaging," *Sensors*, vol. 15, no. 4, pp. 8020–8041, 2015.
[40] F. V. Pop *et al.*, "Novel pMUT-based acoustic duplexer for underwater and intrabody communication," in *Proc. IEEE Int. Ultrason. Symp. (IUS)*, Dec. 2018, pp. 1–4.
[41] S.-R. Kothapalli *et al.*, "Simultaneous transrectal ultrasound and photoacoustic human prostate imaging," *Sci. Transl. Med.*, vol. 11, no. 507, Aug. 2019, Art. no. eaav2169.
[42] A. Hajati, D. Latev, and D. Gardner, "3D MEMS piezoelectric ultrasound transducer technology," in *Proc. Joint IEEE Int. Symp. Appl. Ferroelectr. Workshop Piezoresponse Force Microsc., (ISAF/PFM)*, Jul. 2013, pp. 231–235.
[43] W. Liao *et al.*, "Piezeoelectric micromachined ultrasound tranducer array for photoacoustic imaging," in *Proc. Transducers Eurosens. XXVII, 17th Int. Conf. Solid-State Sensors, Actuat. Microsyst., (TRANSDUCERS EUROSENSORS)*, Jun. 2013, pp. 1831–1834.
[44] H. Ahn, M. Sung, K. Been, and W. Moon, "Design and fabrication of a piezoelectric micromachined ultrasound array transducer for photoacoustic imaging applications," in *Proc. 11th Int. Conf. Ubiquitous Robots Ambient Intell., URAI*, Nov. 2014, pp. 73–76.
[45] B. Chen, F. Chu, X. Liu, Y. Li, J. Rong, and H. Jiang, "AlN-based piezoelectric micromachined ultrasonic transducer for photoacoustic imaging," *Appl. Phys. Lett.*, vol. 103, no. 3, Jul. 2013, Art. no. 031118.
[46] A. Dangi *et al.*, "Evaluation of high frequency piezoelectric micromachined ultrasound transducers for photoacoustic imaging," in *Proc. IEEE Sensors*, New Delhi, India, Oct. 2018, pp. 1–4.
[47] A. Dangi and R. Pratap, "System level modeling and design maps of PMUTs with residual stresses," *Sens. Actuators A, Phys.*, vol. 262, pp. 18–28, Aug. 2017.
[48] A. J. Fox, B. Drawl, G. R. Fox, B. J. Gibbons, and S. Trolier-McKinstry, "Control of crystallographic texture and surface morphology of Pt/Tio$_2$ templates for enhanced PZT thin film texture," *IEEE Trans. Ultrason., Ferroelectr., Freq. Control*, vol. 62, no. 1, pp. 56–61, Jan. 2015.
[49] "American national standard for safe use of lasers," Laser Inst. Amer., Orlando, FL, USA, Tech. Rep. ANSI Z136.1-2007, 2007.
[50] K. M. Smyth, C. G. Sodini, and S.-G. Kim, "High electromechanical coupling piezoelectric micro-machined ultrasonic transducer (PMUT) elements for medical imaging," in *Proc. 19th Int. Conf. Solid-State Sens., Actuators Microsyst. (TRANSDUCERS)*, Jun. 2017, pp. 966–969.
[51] F. Sammoura, S. Akhbari, and L. Lin, "An analytical solution for curved piezoelectric micromachined ultrasonic transducers with spherically shaped diaphragms," *IEEE Trans. Ultrason., Ferroelectr., Freq. Control*, vol. 61, no. 9, pp. 1533–1544, Sep. 2014.

Ajay Dangi (M'18) received the B.Tech. degree in mechanical engineering from IIT (BHU) Varanasi, Varanasi, India, in 2010, and the Ph.D. degree in mechanical engineering from the Indian Institute of Science, Bengaluru, India, in 2016.

From 2016 to 2017, he was a Research Assistant with MEMS Laboratory, Center for Nano Science and Engineering, Indian Institute of Science. Since 2017, he has been working as a Postdoctoral Scholar with the Department of Biomedical Engineering, Pennsylvania State University, University Park, PA, USA. His research interests include photoacoustic and ultrasound imaging, MEMS/MOEMS sensors, piezoelectric micromachined ultrasound transducers (PMUTs), and acoustics.

Christopher Y. Cheng (M'17) received the B.S. degree (*cum laude*) in materials science and engineering and the B.S. degree in chemistry from the University of Minnesota at Twin Cities, Minneapolis, MN, USA, in 2016. He is currently pursuing Ph.D. degree in materials science and engineering with Pennsylvania State University, University Park, PA, USA, with a focus on piezoelectric micromachined ultrasound transducers (PMUTs) and their applications.

He was an Intern at 3M Company, Maplewood, MN, USA, and the U.S. Army Research Laboratory, Adelphi, MD, USA.

Mr. Cheng is a National Science Foundation Graduate Research Fellow Awardee and a National Defense Science and Engineering Graduate Fellow.

Sumit Agrawal received the B.Tech. degree in electronics and communication from the GLA Institute, Mathura, India, in 2012, and the M.Tech. degree in media and sound engineering from IIT Kharagpur, Kharagpur, India, in 2014. He is currently pursuing the Ph.D. degree in biomedical engineering with Pennsylvania State University, University Park, PA, USA.

From 2014 to 2015, he worked as an Applications Development Engineer with KLA Tencor, Chennai, India, where he explored image-processing algorithms for defect inspection in silicon wafers during integrated circuit fabrication. From 2015 to 2016, he worked with SkinCurate Research, Kharagpur, India, a smart medical imaging devices startup, where he developed an interest in medical imaging and machine learning. His current research includes developing dual-modality ultrasound and photoacoustic imaging hardware as well as image reconstruction software.

Sudhanshu Tiwari received the B.Tech. degree in mechanical engineering from A.P.J. Abdul Kalam Technical University, Lucknow, India, in 2015. He is currently pursuing the Ph.D. degree with Centre for Nano Science and Engineering, Indian Institute of Science, Bengaluru, India.

His research interests include PiezoMEMS design, microfabrication, and vibrational analysis of microelectromechanical systems (MEMS) structures.

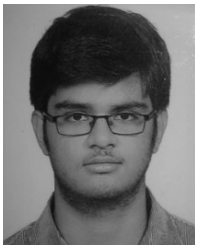

Gaurav Ramesh Datta received the B.Tech. degree in electrical engineering from the College of Engineering Pune, Pune, India, an autonomous institute of Government of Maharashtra affiliated to Savitribai Phule Pune University, in 2016. He is currently pursuing the M.S. degree with Pennsylvania State University, University Park, PA, USA.

He has been working as a Research Assistant at the Biophotonics and Ultrasound Imaging Laboratory, Pennsylvania State University, since May 2018.

Robert R. Benoit (M'10) received the B.A. degree in physics and math from Lycoming College, Williamsport, PA, USA, in 2004 and the M.S. and Ph.D. degrees from the University of Virginia (UVA), Charlottesville, VA, USA, in 2007 and 2014, respectively.

He is currently an Electronics Engineer with Microdevices Devices Branch. U.S. Army Research Laboratory (ARL), Adelphi, MD, USA. At UVA, he studied rapid prototyping of MEMS devices with focused ion beams and cryogenic radio-frequency microelectromechanical systems (RF MEMS) for radio astronomy applications. His current research involves piezoelectric RF MEMS and wafer-scale vacuum packaging techniques.

Dr. Benoit serves as the Chair for the Washington DC/Northern VA Chapter of the Microwave Theory and Technique Society.

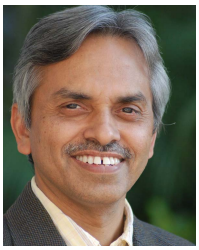

Rudra Pratap (SM'02) received the B.Tech. degree (Hons.) from IIT Kharagpur, Kharagpur, India, in 1985, the M.S. degree from The University of Arizona, Tucson, AZ, USA, in 1987, and the Ph.D. degree from Cornell University, Ithaca, NY, USA, in 1993.

He taught at the Sibley School of Mechanical and Aerospace Engineering, Cornell University, from 1994 to 1996. In 1996, he joined the Department of Mechanical Engineering, Indian Institute of Science, Bengaluru, as an Assistant Professor, where he served full time from 1996 to 2010. He moved to the Centre for Nano Science and Engineering (CeNSE) as a Professor and the Founding Chairperson. He continues as an Associate Faculty Member of mechanical engineering. He has been the Deputy Director of the Indian Institute of Science since August 2018. His research interests include microelectromechanical systems (MEMS) and NEMS, vibroacoustics, bioacoustics, mechanobiology, and computational mechanics.

Dr. Pratap is an elected fellow of the National Academy of Engineering and National Academy of Science. He is an Associate Editor of the IEEE/ASME JOURNAL OF MICROELECTROMECHANICAL SYSTEMS and *Journal of ISSS*.

Susan Trolier-McKinstry (F'91) is currently the Steward S. Flaschen Professor of Ceramic Science and Engineering, a Professor of electrical engineering, and the Director of the Nanofabrication Facility, Pennsylvania State University, University Park, PA, USA. Her main research interests include thin films for dielectric and piezoelectric applications. She has written approximately 400 articles in these areas.

Prof. Trolier-McKinstry is an elected member of the National Academy of Engineering (NAE). She served as the President for the IEEE Ultrasonics, Ferroelectrics and Frequency Control Society and Keramos. She was the President of the Materials Research Society in 2017. She currently serves as an Associate Editor for *Applied Physics Letters*.

Sri-Rajasekhar Kothapalli received the Ph.D. degree in biomedical engineering from Washington University in St. Louis, St. Louis, MO, USA, in 2009.

From 2009 to 2013, he carried out his postdoctoral research at Stanford University, Stanford, CA, USA, where he was an Instructor with the Department of Radiology from 2014 to 2016. His research work spans various biomedical imaging techniques, including photoacoustic imaging, ultrasound imaging, and ultrasound-modulated optical tomography (UOT). Working at the interface of MEMS ultrasound transducer and photoacoustic imaging, he developed a capacitive micromachined ultrasound transducer (CMUT)-based dual-modality transrectal ultrasound and photoacoustic (TRUSPA) imaging device for prostate cancer screening and conducted clinical studies on several prostate cancer patients using the TRUSPA device. He is currently an Assistant Professor with the Department of Biomedical Engineering, Pennsylvania State University, University Park, PA, USA.